Bioactive Materials 6 (2021) 3254–3268

Contents lists available at ScienceDirect

Bioactive Materials

journal homepage: www.sciencedirect.com/journal/bioactive-materials

Construction of nanofibrous scaffolds with interconnected perfusable microchannel networks for engineering of vascularized bone tissue

Jiani Gu, Qianqian Zhang, Mengru Geng, Weizhong Wang, Jin Yang, Atta ur Rehman Khan, Haibo Du, Zhou Sha, Xiaojun Zhou **, Chuanglong He *

State Key Laboratory for Modification of Chemical Fibers and Polymer Materials, College of Chemistry, Chemical Engineering and Biotechnology, Donghua University, Shanghai, 201620, PR China

ARTICLE INFO

Keywords:
3D printing
Microchannel networks
Vascular endothelial growth factor
Vascularization
Bone regeneration

ABSTRACT

Vascularization and bone regeneration are two closely related processes during bone reconstruction. A three-dimensional (3D) scaffold with porous architecture provides a suitable microenvironment for vascular growth and bone formation. Here, we present a simple and general strategy to construct a nanofibrous poly(L-lactide)/poly(ε-caprolactone) (PLLA/PCL) scaffold with interconnected perfusable microchannel networks (IPMs) based on 3D printing technology by combining the phase separation and sacrificial template methods. The regular and customizable microchannel patterns within the scaffolds (spacings: 0.4 mm, 0.5 mm, and 0.6 mm; diameters: 0.8 mm, 1 mm, and 1.2 mm) were made to investigate the effect of microchannel structure on angiogenesis and osteogenesis. The results of subcutaneous embedding experiment showed that 0.5/0.8-IPMs (spacing/diameter = 0.5/0.8) and 0.5/1-IPMs (spacing/diameter = 0.5/1) scaffolds exhibited more vascular network formation as compared with other counterparts. After loading with vascular endothelial growth factor (VEGF), VEGF@IPMs-0.5/0.8 scaffold prompted better human umbilical vein endothelial cells (HUVECs) migration and neo-blood vessel formation, as determined by Transwell migration, scratch wound healing, and chorioallantoic membrane (CAM) assays. Furthermore, the microangiography and rat cranial bone defects experiments demonstrated that VEGF@IPMs-0.5/0.8 scaffold exhibited better performance in vascular network formation and new bone formation compared to VEGF@IPMs-0.5/1 scaffold. In summary, our results suggested that the microchannel structure within the scaffolds could be tailored by an adjustable caramel-based template strategy, and the combination of interconnected perfusion microchannel networks and angiogenic factors could significantly enhance vascularization and bone regeneration.

1. Introduction

In the process of bone growth, development, remodeling and repair, bone formation and vascularization are closely related, and the invasion of blood vessels is a prerequisite for ossification [1]. Traditional bone repair focuses on the formation of new bone, while in the process of bone formation, the early vascularization of new bone is particularly important. The vascular network plays an indispensable role in maintaining the function of most tissues via providing cells with appropriate oxygen and nutrients, while effectively removing metabolic wastes [2–4]. Constructing a bone scaffold with a vascular network can guide cells to grow inward, and sufficient space and nutrient delivery in the scaffold contribute to the formation of blood vessels, which improves the survival rate of the tissue and reduces the failure of bone graft materials *in vivo* [5]. The porous structure of traditional scaffolds is usually relatively simple, mainly providing mass exchange through free diffusion, and the blood vessels grow slowly inward, making it difficult to obtain a functional blood vessel network [6].

Microchannels are simple, perfusable architectural features designed into biomaterials to promote diffusive transport of oxygen and nutrients to surrounding tissues, facilitate effective cell seeding, and control the spatiotemporal distribution of molecules and ligands, and survival, integration and vascularization of tissue analogues *in vivo* [7]. The field of bone regeneration has recently recognized the role of complex

Peer review under responsibility of KeAi Communications Co., Ltd.
* Corresponding author.
** Corresponding author.
E-mail addresses: zxj@dhu.edu.cn (X. Zhou), hcl@dhu.edu.cn (C. He).

https://doi.org/10.1016/j.bioactmat.2021.02.033
Received 15 January 2021; Received in revised form 17 February 2021; Accepted 24 February 2021

information biomaterials, through the modification of their physical and chemical structures, in driving endothelial behavior *in vitro* [8], and the impact of promoting tissue vascularization *in vivo*. For example, several studies have demonstrated the pore shape, porosity and pore size of biomaterials affect angiogenesis and wound healing through structural impact [9,10]. A previous study demonstrated the response of endothelial cells to topological cues (such as nano and microgrooves or patterns) on the surface of two-dimensional materials [11,12]. Biomaterial scaffolds with well-vascularized large pores, more than 300 μm [13], and porosity greater than 50% are preferred as bone replacement implants because they have a good angiogenic capacity and can lead to direct osteogenesis (without preceding cartilage formation) [13].

In the past few years, approaches of introducing hollow, perfusable microchannels into 3D biomaterial scaffolds have been widely pursued. For example, scaffolds are cast around wire or needle templates, leading to hollow, perfusable microchannels in the scaffolds when templates are removed after manufacture [14,15]. These conventional methods are simple and accessible but usually limited in the size and final spatial structure of microchannels because of their low accuracy and poor control. 3D printed scaffolds have received extensive attention in tissue engineering in the past few decades because of their unique three-dimensional porous microchannel structures and high precision, especially in bone tissue engineering.

Numerous attempts have been made to induce the growth of the vascular system within 3D engineered tissue structures [16–18]. Stevens et al. developed a general 3D bioprinting strategy to solve the problems of maintaining structural fidelity and effective endothelialization and tissue vascularization [19]. However, this method does not involve microchannel studies and *in vivo* verification. Shao et al. reported that a novel 3D bioprinting method with hydrogels can directly print millimeter-level fine nutrient delivery channels and achieved the purpose of effective vascularization [20]. Compared with other reported bioprinting methods, their bioprinting strategy described here can guarantee both the printability of large free-form constructs and the achievability of biological performance. However, hydrogels are not strong enough to maintain long-term tubular structures under pressure. Lei et al. established a new strategy based on 3D printing technology to achieve an efficient bionic construction of a vascular network [21]. First, a caramel-based 3D printing template was prepared and a thin polymer was coated on it. During solvent evaporation, the microstructure of the polymer coating was adjusted based on the phase separation mechanism. Finally, the sacrificial template was removed to form a layered microchannel network. However, further research on the relationship between the tunable microchannel networks and vascularization needs to be emphasized. At present, few studies discuss the effect of different diameters of microchannels in the scaffold on tissue regeneration. Therefore, it is very important and necessary to understand how the vascular network structure of the scaffolds affects blood vessel formation and bone regeneration [22].

To overcome the above obstacles, herein we established a 3D printed sacrificial caramel-based template strategy to create an interconnected perfusable microchannel networks (IPMs) within nanofibrous scaffolds, and investigated the effects of microchannel structure on vascularization and osteogenesis. The Poly(L-lactide)/poly(ε-caprolactone) (PLLA/PCL) nanofibrous scaffold with interconnected porous architecture was used in this study since it can be fabricated without using sacrificial porogen [23]. At the same time, the microstructure allowed the permeation of nutrients through the scaffold which was beneficial to the tissue ingrowth. This strategy could be readily applied to various polymers, and by adjusting the caramel template, tunable scaffolds with different specifications (spacings: 0.4 mm, 0.5 mm, and 0.6 mm; diameters: 0.8 mm, 1 mm, and 1.2 mm) can be fabricated. However, scaffolds with only microchannels cannot significantly promote vascularization effectively. Vascular endothelial growth factor (VEGF), the most commonly used growth factor in bone tissue engineering in the past few decades, is effective to improve vascularization via angiogenesis [24]. Therefore, the VEGF was loaded in the hydrogel (aldehyde hyaluronic acid/-carboxymethyl chitosan) and perfused in the microchannel scaffold, so that the microchannel structure and the inducing factor can interact with each other to repair the bone defect. We demonstrated the effect of microchannel structure on angiogenesis and osteogenesis by cultivating human umbilical vein endothelial cells (HUVECs) *in vitro* and angiogenesis and osteogenesis *in vivo* during the microangiography and rat cranial bone defects experiments.

2. Materials and method

2.1. Materials

Poly(ε-caprolactone) (PCL) (Mn: 80000), tetrahydrofuran (THF), sodium periodate ($NaIO_4$), dexamethasone, L-ascorbic acid, and β-glycerol phosphate were purchased from Sigma-Aldrich Trading Co., Ltd. (Shanghai, China). Sucrose (purity ≥ 99.9%) was obtained from Aladdin Reagent Co., Ltd. (Shanghai, China), and poly(L-lactide) (1.93 dL/g intrinsic viscosity) was provided by Daigang Biomaterials Inc. (Jinan, China). Sodium hyaluronate was purchased from Liuzhou Dali Biotechnology Co., Ltd. (Guangxi, China). Carboxymethyl chitosan (CMCS) was sourced from Shanghai Bangcheng Biotechnology Co., Ltd. (Shanghai, China). Recombinant Human VEGF165 (rhVEGF165) was purchased from Peprotech. (New Jersey, USA). Human VEGF Quantikine ELISA Kits were obtained from Shanghai Zcibio Technology Co., Ltd. (Shanghai, China). Fetal bovine serum (FBS), DMEM/F12, RPMI medium 1640, penicillin-streptomycin, and trypsin were purchased from Gibco Life Technologies Co. (Grand Island, USA).

2.2. Fabrication and characterization of sacrificial caramel-based template

Sucrose (purity ≥ 99.9%) was used as raw materials for 3D printing. Sucrose granules were preheated to 180 °C for about 15–20 min in the muffle furnace (FO311C; Yamato Scientific, Japan) to make them moderately caramelized and amber. After cooling to the solid-state, the caramel solid was preheated to 120–130 °C in the extrusion cavity of a rapid prototyping manufacturing system (HTS-400; Fochif Mechatronics Technology, China) for several minutes, depending on the previous caramelization degree. The molten caramel was extruded out through a nozzle with the temperature of 125–130 °C and directly deposited on a plate to form a 3D sacrificial caramel template according to the expected pattern [21]. The filaments of caramel templates with different diameters and spacings were designed. The selected needle diameters were 0.4 mm, 0.5 mm, and 0.6 mm. The grid width (center-to-center distance) between filaments was 0.8 mm or 1 mm or 1.2 mm with −45°/45°or 0°/90° lay-down patterns between two successive layers. The height of each layer was 0.4 mm, 0.5 mm, and 0.6 mm according to the diameter of the needle. To obtain a template with better morphology and avoid stacking or breaking between layers, the extrusion rate was adjusted in the range of 0.001–0.03 mm/s. 3D printed caramel templates were imaged by optical microscope (IX71, Olympus, Japan). For compression test, the template was measured by a universal mechanical tester (HY–940FS, Shanghai Hengyu Co., Ltd., China) with a 200 N sensor. The sample was compressed to destruction at a speed of 1 mm/min. All measurements were performed in triplicate.

2.3. Construction and characterization of IPMs-PLLA/PCL scaffold

The IPMs scaffold was fabricated by combining our previously described thermally induced phase separation (TIPS) technique [23] with 3D printed caramel-based templates. Briefly, the blends of PLLA and PCL with a weight ratio of 70:30 were first dissolved at 60 °C in THF under magnetic stirring for 1–2 h to obtain homogeneous polymer solutions of 10% (w/v). Next, the obtained homogeneous polymer solutions were immediately casted into 3D-printed caramel-based templates.

After casting, they were quickly placed at −80 °C for at least 4 h. Afterward, the polymer gels with 3D printed caramel-based templates were taken out and then immersed into an ice/water mixture for 4–5 days to completely eliminate caramel and residual solvent. The water was changed three times per 24 h. Finally, the IPMs scaffold was obtained by removing from the water and freeze-drying for 48 h.

The morphology and microstructures of IPMs scaffold with different specifications were observed by a scanning electron microscope (SEM, Phenom XL, China). The samples were dried by a vacuum freeze dryer (ALPHA 1–2 LD, Germany), and the cross-section of the scaffolds was quenched with liquid nitrogen. Before observation, the surfaces of samples were sprayed with gold and then characterized using SEM at an acceleration voltage of 10 kV. For compression testing, IPMs scaffold was tested by a universal test system with a 200 N sensor. The sample was compressed to a large strain of 80% at a speed of 1 mm/min. The modulus was calculated by taking the initial slope of the stress-strain curve. All tests were repeated with six specimens.

2.4. Preparation of VEGF@IPMs scaffold

2.4.1. Synthesis of aldehyde hyaluronic acid (A-HA)

A-HA was synthesized with some modification based on the previously reported method [25]. Briefly, 5 g HA was dissolved in 500 mL ultrapure water at a concentration of 10 mg/mL under magnetic stirring to obtain homogeneous solutions. Next, 1 g sodium periodate was dissolved in 5 mL ultrapure water in the dark at room temperature. An aqueous solution of sodium periodate was added into the HA solution dropwise, and the reaction was stirred for 24 h under dark conditions. Then, 2 mL ethylene glycol was added to stop the reaction by inactivating any unreacted periodate and the solution was stirred for 1 h at ambient temperature. Subsequently, the obtained reaction solution was transferred to a dialysis bag (MWCO 7000, Viskase, USA) and purified by exhaustive dialysis for 3 days, with the deionized water being changed 4 times per 24 h. The dry product was obtained by freeze-drying for 2 days for further use.

2.4.2. Preparation of VEGF loaded hydrogels

CMCS) and A-HA can be blended to form injectable hydrogel via Schiff's base reaction, and the preparation process is simple and gentle [26]. Therefore, the CMCS/A-HA hydrogels are available for VEGF loading within the IPMs scaffolds. CMCS (6%, w/v) and A-HA (6%, w/v) were dissolved in phosphate-buffered saline (PBS) separately. The crosslinked composite hydrogels were formed by mixing CMCS and A-HA solutions at an equal volume at room temperature.

The rhVEGF165 was incorporated non-covalently in the hydrogels by pre-mixing VEGF in A-HA (6%, w/v) with PBS homogeneous solution before crosslinking [27]. Then, the hydrogel was infused into IPMs scaffolds through micropipette tip.

2.5. Porosity test

The porosity of scaffolds was measured by the liquid displacement method [28]. Anhydrous ethanol was selected as the replacement liquid due to its ability to seep into the internal pores of PLLA/PCL without dissolution, swelling, or shrinkage of the scaffolds [29]. Briefly, the cylindrical sample with a dry weight (W_1) was immersed in absolute ethanol, and placed in a vacuum drying oven to circulate vacuum processing until no bubbles were generated in the holder. Then scaffolds were removed from the ethanol, wiped off the excess ethanol on the surface, and weighed the weight (W_2). The porosity of the sample was calculated by the following formula:

$$\text{Porosity}(\%) = \frac{W_2 - W_1}{\rho V} \times 100\%$$

Where ρ is the density of the ethanol at room temperature, V is the volume of the wet IPMs scaffold, which is directly calculated by measuring the diameter and height of the cylindrical scaffolds. Values were expressed as mean ± standard deviation (n = 3) [23].

2.6. In vitro release kinetics of growth factors

For *in vitro* release study, VEGF was released from scaffolds in PBS at pH 7.4. Scaffolds loaded with VEGF (1 μg) were placed into the centrifuge tubes containing 5.0 mL PBS and incubated in a thermostatic shaker at 37 °C with a speed of 100 rpm. At 6, 12, 24, 48, 72, 96, 120, 168, 240, and 336 h, the release medium was withdrawn and replaced with an equal volume of fresh medium to ensure the total volume. Released amounts of VEGF was quantified with sandwich enzyme-linked immunosorbent assay (ELISA), using a commercially available kit [27]. All measurements were performed in triplicate.

2.7. Cells culture

HUVECs were obtained from the Cell Bank of the Chinese Academy of Sciences and cultured in a RPMI-1640 medium containing 10% (v/v) fetal bovine serum (FBS) and 1% (v/v) penicillin/streptomycin at 37 °C in the incubator with 5% CO_2. The culture media was changed in 2 days intervals. Bone marrow mesenchymal stem cells (BMSCs) were obtained from a 2-week-old male Sprague-Dawley (SD) rat purchased from Shanghai JSJ Laboratory Animal Co., Ltd., China. First, the femurs and tibias of the SD rat's hind leg were removed, and then the bone marrow in the bone marrow cavity was washed out with a DMEM/F12 medium containing 10% (v/v) FBS and 1% (v/v) penicillin/streptomycin. BMSCs were cultured at 37 °C in a humidified CO_2 (5%) cell incubator, and the cell culture medium was replaced every 2 days. The 3-5th generation cells with a better growth state were selected for subsequent experiments. All animal procedures were performed following local animal welfare laws and guidelines, and were approved by the Animal Ethics Committee of Donghua University.

2.8. Cell viability assay

The viability of HUVECs on the scaffold was evaluated by Cell Counting Kit-8 (CCK-8). The sterilized 0.4/1, 0.5/0.8, 0.5/1, 0.5/1.2 and 0.6/1 scaffolds (spacing/diameter) were placed in 48-well plates, and the control group was a blank culture plate without samples (TCP). HUVECs were seeded on the scaffolds at 2×10^4 cells per well. The medium was changed every 2 days. After culturing for 1, 4, and 7 days, the medium was removed and the scaffolds were washed 3 times with PBS. Next, 200 μL of CCK-8 working solution containing 10% CCK-8 reagent was added to each well. After incubating for 1 h at 37 °C in a 5% CO_2 incubator, 100 μL of supernatant was transferred to a 96-well plate, and the absorbance was read at 450 nm by a microplate reader (MK3, Thermo, USA). Next, to visually observe the growth of the cells, the nucleis on the surface of the scaffold were stained with DAPI and observed and photographed with a fluorescence microscope (IX71, Olympus, Japan).

Subsequently, HUVECs were seeded on IPMs scaffolds with a certain thickness, with the purpose of studying the ability of cells to grow into the scaffold microchannel. HUVECs were seeded on the scaffold with 5×10^4 cells per well. After 7 days of culture, the medium was removed, and the scaffold was washed 3 times with PBS. HUVECs were incubated with 0.1% Triton X-100 for 5 min, fixed with 4% paraformaldehyde for 15 min, and incubated with 1% bovine serum albumin (BSA) in PBS for 30 min. The actin filaments of HUVECs were stained with Alexa Fluor 488- phalloidin for 30 min, and the nucleus was stained with DAPI for 10 min.

2.9. Transwell migration assay

The migration of HUVECs was evaluated with a Transwell system

(Corning Costar, MA, USA) including an 8 μm polycarbonate filter inserted in a 24-well plate [30]. Briefly, HUVECs were harvested with trypsin in RPMI-1640 containing 10% (v/v) FBS and 1% (v/v) penicillin/streptomycin. Next, IPMs scaffolds of different specifications (0.5/0.8, 0.5/1) loaded with different concentrations of VEGF (0 ng/mL, 200 ng/mL, 500 ng/mL) were added to each well in the lower chamber. Subsequently, 600 μL of serum-free RPMI-1640 culture medium was added to the lower chamber, and then 2×10^4 HUVECs were seeded to the upper chamber. After 24 h of incubation, the cells at the bottom of the Transwell membranes were rinsed with PBS twice and fixed with 4% paraformaldehyde at 4 °C for 30 min. After carefully erasing non-migrating cells in the upper cavity with a cotton swab, Transwell membranes were stained with 1% crystal violet for 10 min. The membranes were washed three times with PBS and photographed under an inverted microscope. Finally, the crystal violet was dissolved in 10% acetic acid, and the absorbance was measured at 590 nm. The amount of cell migration was determined as the ratio of the OD values of the treatment relative to the control. Each treatment was repeated in three independent chambers [31].

2.10. Scratch wound assay

An *in vitro* scratch test was performed to measure the unidirectional migration of HUVECs [32]. Green fluorescence protein (GFP) expressed HUVECs were received from Orthopedics Research Institute of Zhejiang University. HUVECs were cultured in a 24-well plate at 37 °C in RPMI 1640 medium containing 10% FBS, and maintained overnight in a humidified incubator (5% CO_2). Cells were seeded at a density of 5×10^4 cells per well. After the cells reaching 80% confluence, the scratch wound was carefully created by using a 200 μL micropipette tip. Then cell debris were removed by washing with PBS. Subsequently, the serum-free RPMI medium was added with IPMs scaffolds with different concentrations of VEGF for 72 h to obtain the extracts. Cell images for each condition were photographed with an inverted fluorescence microscope at 0, 24, and 48 h, and measured the width with ImageJ software [33]. These experiments were performed in triplicate.

2.11. Chicken chorioallantoic membrane (CAM) assay

The *in vivo* biological activity of VEGF released from the hydrogels was evaluated by the CAM analysis of open-shell chickens [34]. Briefly, eggshells from 5-day-old native chicken eggs were wiped with a 75% alcohol cotton ball to disinfect, and fertilized chicken embryos were incubated at 37.5 ± 0.5 °C with 55–65% humidity for 3 days. The eggs were turned twice a day to promote amniotic movement, prevent embryos from adhering, and ensure oxygen supply. On the third day of incubation, the 8-day-old chicken embryos were randomly divided into seven groups: (1) 0.5/0.8 hydrogel; (2) 0.5/1 hydrogel; (3) 0.5/0.8 hydrogel + 500 ng/mL VEGF; (4) 0.5/1 hydrogel + 500 ng/mL VEGF; (5) 0.5/0.8 hydrogel + 1000 ng/mL VEGF and (6) 0.5/1 hydrogel + 1000 ng/mL VEGF. After sterilizing the eggshells with 75% alcohol, the chorioallantoic membranes were opened in a super clean table to place different scaffolds. The inner shell membrane was rinsed with 1 mL of warm saline for 1 min to wet the inner shell membrane of the chicken embryo, and then a syringe needle was used to gently prick a small hole in the inner shell membrane. Subsequently, the inner shell membrane was gently removed with ophthalmic forceps to expose the underlying CAM membrane. Finally, the window was wrapped with parafilm, and the eggs were continued to incubate after labeling. During the incubation, the windows were facing upwards and no more eggs were transferred. After 48 h, the angiogenesis effect surrounding the scaffolds was observed and photographed using a stereo microscope, and the ratio of blood vessel area was measured by Image-Pro Plus software. These experiments were performed in triplicate.

2.12. In vitro osteogenic differentiation and angiogenesis assay

To thoroughly examine and determine the level of osteogenic differentiation and angiogenesis in the different groups, real-time PCR analysis was performed in each group (control group, without and with VEGF group). Briefly, the sterilized IPMs scaffold was placed in 6-well plates, and BMSCs were seeded into the wells at a density of 2×10^5/well. BMSCs were cultured in osteoinduced medium (DMEM/F-12 containing 100 nM dexamethasone, 10 mM β-glycerophosphate, and 50 μg/mL L-ascorbic acid) for 7 or 14 days. The total RNA of BMSCs was extracted with TRIzol reagent. RT-PCR was used to detect the expression of osteogenic and angiogenesis markers, including runt-related transcription factor 2 (RUNX2), osteocalcin (OCN) and osteopontin (OPN), collagen type I (Col I), Vascular Endothelial Growth Factor Receptor 2 (VEGFR2), and von Willebrand factor (vWF). These experiments were performed in triplicate. The forward and reverse primer sequences used in this study are shown in Table S1.

2.13. Evaluation of angiogenesis in vivo

The angiogenesis *in vivo* was evaluated with subcutaneous embedding. Samples were embedded under the skins of four-week-old male ICR mice. All materials were sterilized by ethylene oxide in advance, and all surgical instruments were sterilized by autoclaving in advance. The samples were divided into four groups: (1) 0.5/0.8 hydrogel; (2) 0.5/1 hydrogel; (3) 0.5/0.8 hydrogel + 1 μg VEGF; and (4) 0.5/1 hydrogel + 1 μg VEGF. The mice were randomly divided into 5 groups with 6 mice in each group. Subsequently, the mice were anesthetized by intraperitoneal injection of sodium pentobarbital. The hair on the experimental site of the mice's back was removed and different materials were implanted in the skin. After a predetermined period, materials were obtained for fixation, and images were taken with a stereo microscope to observe the vascular growth. Subsequently, hematoxylin/eosin staining (H&E) and immunofluorescence staining were performed on the sections of the materials in each group to observe the biocompatibility and analyze the angiogenesis *in vivo*. All staining results were observed and photographed under a microscope. Similarly, for the determination of IPMs scaffolds with better angiogenesis, IPMs scaffolds with different specifications (0.4/1, 0.5/0.8, 0.5/1, 0.5/1.2, and 0.6/1) were also investigated with subcutaneous experiment.

2.14. Microangiography

After 4 weeks, the animals were anesthetized by injection of pentobarbital, and Microfil® (Flow Tech, MA) was used for microangiography. After midline thoracotomy, the heart was exposed and cannulated by a vascular catheter, which was fixed by dripping bio glue. Heparinized saline solution (50 mL) was perfused to prevent blood coagulation and clear the vessels of blood, and 4% paraformaldehyde solution was injected to fix the tissue. Then the blue liquid, radioopaque, low viscosity polymer Microfil® was perfused at a flow rate of 2 mL/min, until the tail and toes turned blue. After the compound was polymerized in about 2 h, the implant was removed and fixed in a 4% paraformaldehyde solution for micro-computed tomography (Micro-CT) imaging system (SkyScan 1176, Bruker Optik GmbH, Belgium).

2.15. In situ bone repair

The bone repair efficiency of different materials was evaluated using the previously reported rat critical-size skull defect model [35]. The implants were divided into five groups: (1) blank; (2) 0.5/0.8 hydrogel; (3) 0.5/1 hydrogel; (4) 0.5/0.8 hydrogel + 1 μgVEGF; (5) 0.5/1 hydrogel + 1 μg VEGF. Four-week-old male SD rats were anesthetized with pentobarbital sodium injection intraperitoneally, and 5 mm diameter defects were created on the skull. Then five groups of scaffolds were implanted at the defect site. After 4 and 12 weeks of surgery, the

rats were sacrificed and the skulls were harvested and fixed with 4% paraformaldehyde for further characterization. Micro-CT analysis was performed to observe the degree of bone repair of different scaffolds and the ratio of new bone volume to total volume (BV/TV) was analyzed by CT-Analyzer software. Subsequently, the bone tissue was decalcified for about one month and paraffin-embedded sections were cut into slices for staining. The new bone formation was observed by H&E staining, Masson trichrome staining, and immunofluorescence staining of OCN and OPN; the angiogenesis around the new bone tissue was observed by immunofluorescence staining of platelet endothelial cell adhesion molecule-1 (CD31) and Alpha-smooth muscle actin (α-SMA). Signal intensities were quantified using Image-Pro Plus software. These experiments were performed in triplicate.

2.16. Statistical analysis

All data in this study were presented as mean ± standard deviation (SD) for $n \geq 3$ and performed using one-way analysis of variance (ANOVA) followed by Tukey's method. The statistical significance of all tests was considered at $^{*}P < 0.05$ and $^{**}P < 0.01$.

3. Result and discussion

3.1. Preparation and characterization of IPMs scaffolds

3.1.1. The preparation of IPMs scaffolds

The fabrication process of IPMs scaffolds is shown in Fig. 1A. The melting temperature of sucrose is around 185 °C. However, the high temperature causes the viscosity of small molecules to be too low to maintain a stable form [21]. Therefore, we did not directly perform fused deposition 3D printing on sucrose itself. After preheating sucrose in the muffle furnace, we extended the heat treatment range of sucrose. Through polymerization and aldol condensation, a relatively high molecular weight caramel is produced, making the printing performance stable [36]. The macro picture of pre-caramelization is shown in Fig. S1. By pre-caramelizing sucrose, we printed 3D caramel templates with different diameters and spacings. From the optical micrographs (Fig. 1B–F), we can observe that the printed caramel templates exhibited a certain size. The printing process (Fig. 1G, Video 1) showed that the template had good stability, and the representative photo of a single caramel sacrificial template is shown in Fig. 1H. The compression test of the multi-layered caramel sacrificial template (Fig. 1I) shows that the caramel sacrificial template exhibited a high modulus and low compressive fracture strain, which ensuring structural stability and providing a morphological and structural guarantee for the subsequent construction of IPMs scaffold.

Supplementary video related to this article can be found at https://doi.org/10.1016/j.bioactmat.2021.02.033

In the existing nanofiber preparation technology, thermally induced phase separation (TIPS) is a common method in which temperature changes drive phase separation to prepare polymer nanofibers. Studies have shown that TIPS porous scaffolds can mimic the structural characteristics of natural bone in terms of fiber size, pore size, and porosity [37]. It is found that when the binary polymer system containing L-polylactic acid (PLLA) undergoes phase separation and the two polymers are thermodynamically incompatible, macroporous nanofiber structures can be formed, such as PLLA/PCL composite.

TIPS technology was used to prepare the composite scaffold of PLLA/PCL and caramel frame. After immersing it in ice water for 3–4 days, sacrificial caramel-based filaments were readily dissolved out to form an interconnected perfusable scaffold. At that time, the IPMs scaffold presented a pore structure inside, and the connected pore structure can be perfused with growth factors-loaded hydrogel, which is conducive to vascular growth. As shown in Fig. 2, the position of the original caramel

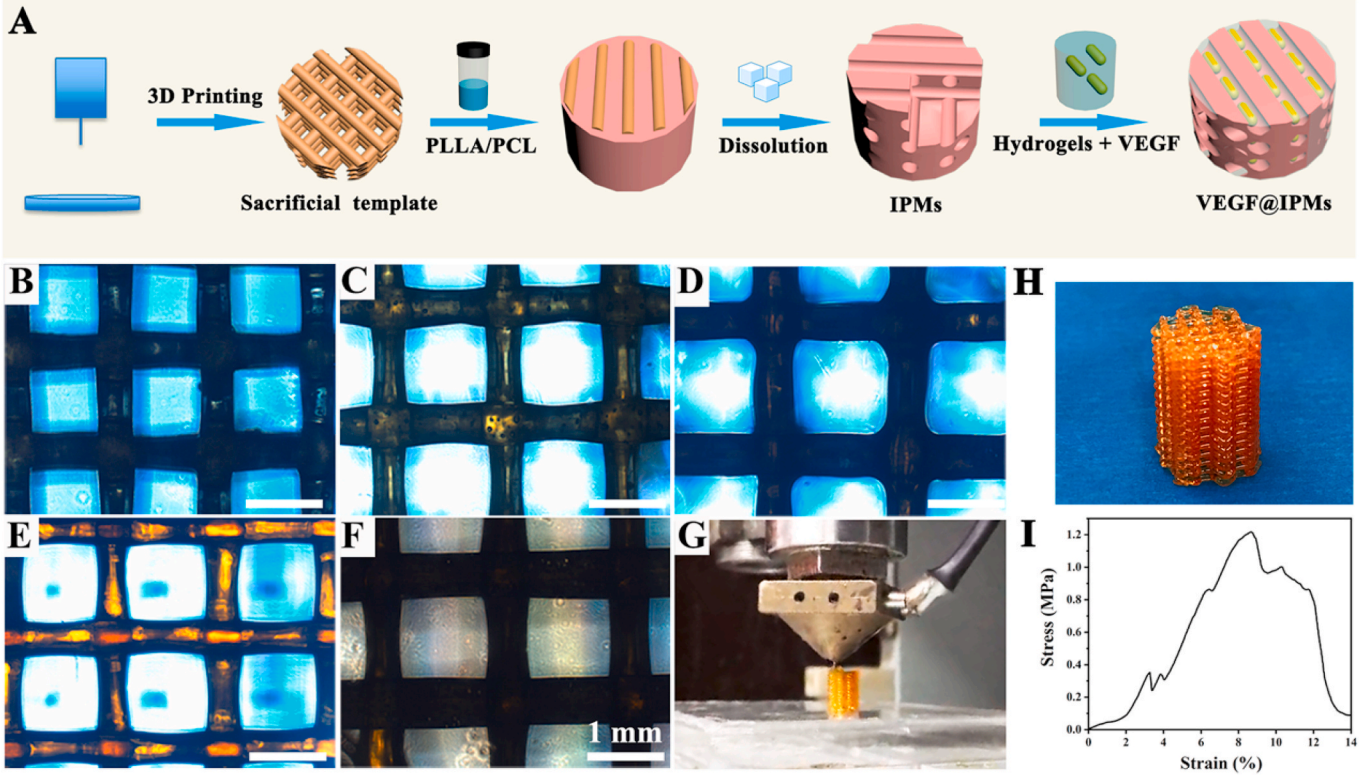

Fig. 1. Schematic illustration and characterization of caramel sacrificial templates. (A) Schematic illustration of the fabrication process for IPMs scaffolds. (B–F) Optical images of caramel sacrificial templates prepared with different nozzle diameters and filament spacing: (B) 0.5/0.8 mm; (C) 0.5/1 mm; (D) 0.5/1.2 mm; (E) 0.4/1 mm and (F) 0.6/1 mm. (G) 3D printing process for caramel sacrificial template. (H) The representative photograph of caramel sacrificial templates. (I) Representative stress-strain curve of caramel sacrificial template in the compression testing.

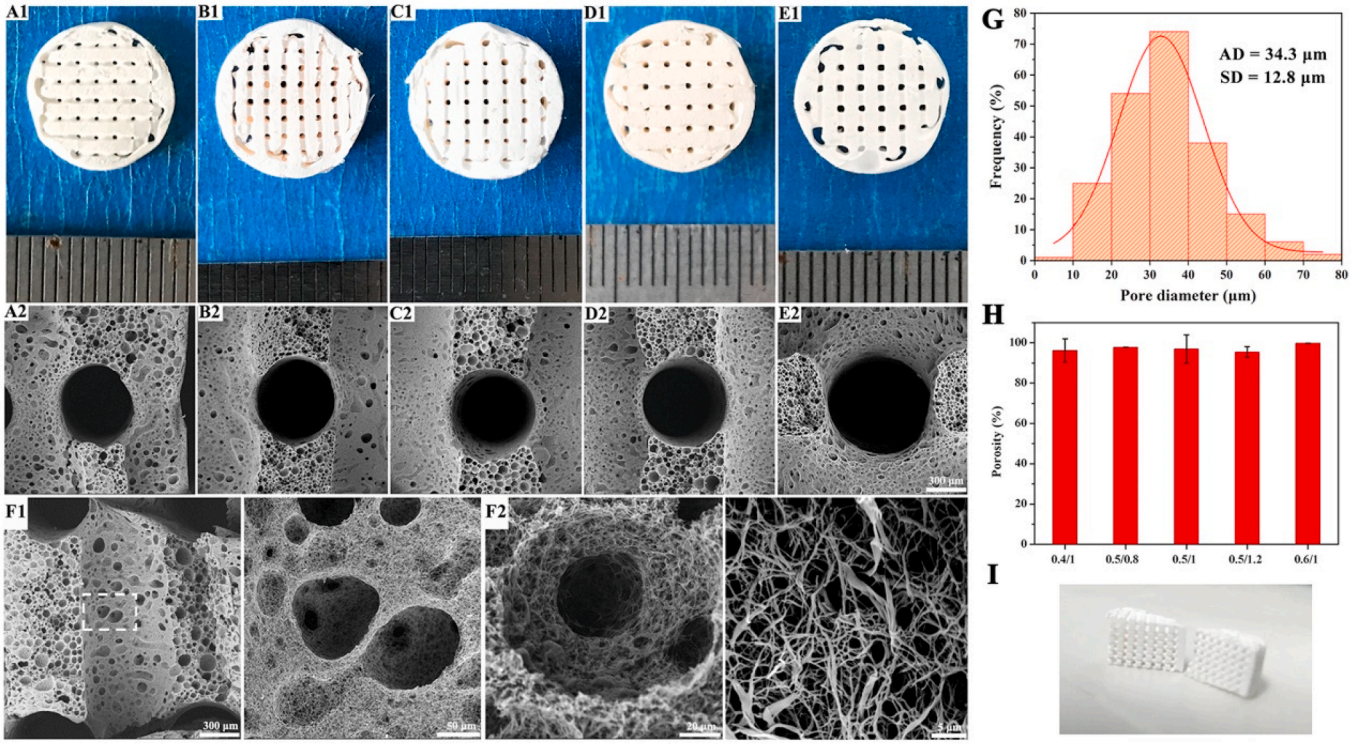

Fig. 2. Morphology and characterization of IPMs scaffolds. (A1-E1) Photographs of IPMs scaffolds prepared with the following combination of specific filament spacing (mm) and diameter (mm): (A1) 0.4/1; (B1) 0.5/0.8; (C1) 0.5/1; (D1) 0.5/1.2 and (E1) 0.6/1. (A2-E2) SEM images of IPMs scaffolds corresponding to (A1-E1). (F1, F2) SEM images of IPMs scaffolds prepared with filament spacing and diameter of 0.5/1 and their magnified fields. (G) Pore diameter distribution of IPMs scaffolds prepared with filament spacing and diameter of 0.5/1, AD indicates the average diameter; SD means the standard deviation. (H) The porosity of IPMs scaffolds prepared from different parameters. (I) The representative photograph of a longitudinal section of IPMs scaffolds.

template holder formed microchannels, and the original gap of the caramel template was filled with the PLLA/PCL solution. The SEM images in Fig. 2A2-F2 clearly revealed the morphologies of IPMs scaffolds. The IPMs scaffold had a spherical macroporous structure, which was related to the existence of PCL. The macropores were interconnected with the average pore size of 34.3 ± 12.8 μm (Fig. 2G). As shown in Fig. 2F2, the magnified SEM image shows that the IPMs scaffold was composed of nanofibers with an average fiber diameter of 256.9 ± 90.6 nm (Fig. S2), which mimics the size of collagen fibers in the native extracellular matrix (ECM) (50–500 nm in diameter) [38]. The porosity of all specifications of the scaffold was above 90% (Fig. 2H). The IPMs scaffold prepared by the sacrificial template method not only exhibits the nanofiber network structure of the biomimetic ECM, but also has a connected microporous structure that facilitates the transportation of nutrients and vascularization.

3.1.2. The evaluation of IPMs scaffolds

(1) Mechanical characterization

In the wet state, mechanical tests were performed on different IPMs scaffolds (Fig. 3). The results showed that under the same diameter, the smaller the spacing, the smaller the compressive modulus value, and there were significant differences among the 0.5/1, and 0.4/1, and 0.6/1 groups (Fig. 3A2). For the 0.4/1 group, the lowest compressive modulus (0.19 MPa) was mainly due to the smallest pore size, which resulted that in the most channels in the same mold and thereby causing the loose network. Under the same spacing, the larger the diameter, the larger the compressive modulus was. The compressive modulus of 0.5/1.2 group was significantly higher than that of 0.5/0.8 and 0.5/1 group (Fig. 3B2). For the 0.5/0.8 group, which possessed the smallest diameter and the most channels prepared in the same mold, formed with the loose network structure, exhibited relatively lowest compressive modulus (0.22 MPa). From the mechanical test results, the compressive mechanical strength of the prepared IPMs scaffolds is relatively low due to the formation of microchannels inside the scaffold. In order to meet the need for scaffold mechanical strength in various bone defect treatments, further research needs to establish a good balance between the mechanical strength of the scaffold and the microchannel structure.

(2) *In vitro* evaluation of IPMs scaffolds

For *in vitro* studies, HUVECs were used to evaluate the proliferation ability of different IPMs scaffolds. After 7 days of culture, it was observed that cells showed the proliferation trend after being cultured on different scaffolds, indicating that each scaffold had good biocompatibility. Among the five groups, the 0.4/1 group showed the best proliferation effect ($p < 0.05$), followed by the 0.5/1 group (Fig. 4B).

(3) Subcutaneous embedding

To visually observe the growth of the cells, the nucleis on the surface of the scaffolds were stained with DAPI and observed using a fluorescence microscope. This was consistent with the results of the CCK-8 test (Fig. S3). Subsequently, HUVECs grew on the IPMs scaffolds were further observed by SEM. As shown in Fig. 4A, the cells grew on the surface of the scaffolds showed spreading morphology. As the culture time increased, the number of cells on the surface of the scaffold also increased. The above results further confirmed that all the fabricated scaffolds had good biocompatibility and supported cell growth.

To further investigate the ability of cells to grow into the pores of the scaffolds, HUVECs were seeded on different scaffolds with a certain thickness and then cultured on a culture plate with low cell adhesion. IPMs scaffolds were cut by a blade to obtain a longitudinal section,

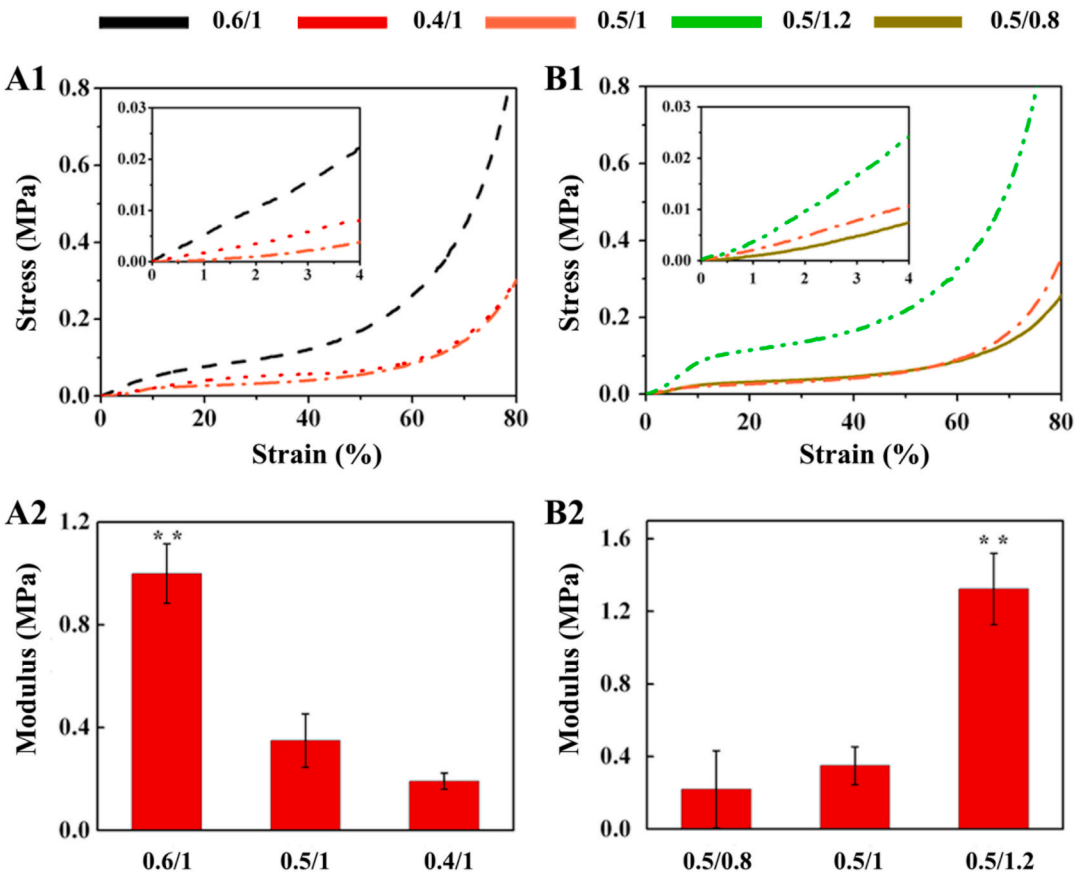

Fig. 3. Compressive mechanical behavior of IPMs scaffolds prepared with different filament spacing and diameter. (A1, B1) The representative stress-strain curves. (A2, B2) Young' modulus. **P < 0.01 compared with other groups.

which was observed through a fluorescence microscope. From Fig. 4D, different cell numbers and different cell distribution depths inside different scaffolds can be observed.

In the 0.4/1 group, due to the small pore size, most of the cells were trapped and grown on the surface of the scaffold. A small number of cells entered the scaffold, and the depth of distribution of cells inside the scaffold was the smallest. In different scaffold groups (0.5/0.8, 0.5/1, 0.5/1.2) with a pore size of 0.5, more cell growth was seen within the scaffold. Specifically, the cells in the 0.5/1 group basically penetrated the entire scaffold, and the cells in the 0.5/0.8 group sneaked in half and stayed in the middle channel, but the upper channel had been fully covered and connected. When the pore size increased to 0.6, though the cells were distributed in a better depth inside the scaffold, the cells of the 0.6/1 group gathered in the left half of the middle layer, and the number of cells decreased. This may be due to the larger pore size making it easy to leak and difficult to trap more cells inside the scaffold.

The subcutaneous embedding experiment was carried out to further investigate the tissue growth in different scaffolds. The optimal IPMs scaffolds can be selected by *in vitro* experiments. Fig. 5 shows the distribution of capillary vessels on the surface of the scaffolds and the H&E staining image after the scaffolds were embedded subcutaneously in ICR mice for one month. As shown in Fig. 5A, the images obtained from stereomicroscope showed that the vascular tissue of the surface of the scaffold in the 0.5/0.8 group and 0.5/1 group was more abundant. As shown in Fig. 5B, C, D, the H&E staining images clearly showed the cross-section of small blood vessels (indicated by arrowheads), which was consistent with the results of the stereomicroscope images. In summary, after combining physical characterization (mechanical characterization), *in vivo* (subcutaneous embedding), and *in vitro* (cell behavior) experiments, finally we selected the 0.5/0.8 and 0.5/1 groups as suitable specifications for subsequent experiments due to comprehensive consideration [13,39].

3.2. Promotion of microvasculature growth by IPMs scaffolds loaded with VEGF

Before evaluating the effect of VEGF@IPMs scaffold on bone repair *in vivo*, we first investigated the ability of VEGF@IPMs scaffold to promote angiogenesis. The release rate of VEGF from VEGF@IPMs scaffold was also measured. As shown in Fig. S4B, the initial rapid release of VEGF from 0.5/0.8 and 0.5/1 scaffolds in the first 24 h was similar. On day 7, the former was higher than the latter, reaching 50.00 ng/mL and 47.34 ng/mL respectively. The previous study had revealed that days 7 post-operatively was a critical time points for vascularization of bone injury [40]. Then, both scaffolds continued to release VEGF for the next 7 days. The VEGF was released as the hydrogels degraded by comparing the release profile with the weight loss curve (Fig. S4C).

It is a well-known fact that endothelial cell migration is a key process of angiogenesis. The first step of vascularization is the recruitment of endothelial cells to facilitate the formation of new blood vessels. Therefore, we used a cell migration chamber to test whether the VEGF-loaded IPMs scaffolds can induce HUVECs migration in a serum-free medium. As shown in Fig. 6A, the scaffolds with a low concentration of VEGF (200 ng/mL) effectively induced HUVECs to migrate from the upper surface of the membrane to the lower surface, as compared with the scaffolds without VEGF loading. The higher the concentration of growth factors, the stronger the ability to induce cell migration, and the more cells adhered to the lower surface of the Transwell membrane. Dissolved crystal violet was used to further quantitatively analyze cell migration. It was observed that OD values of the 0.5/0.8 group and the 0.5/1 group, which loading with 500 ng/mL VEGF, were higher (0.1089 ± 0.0086 and 0.0952 ± 0.0052) than those of other groups. The 0.5/0.8

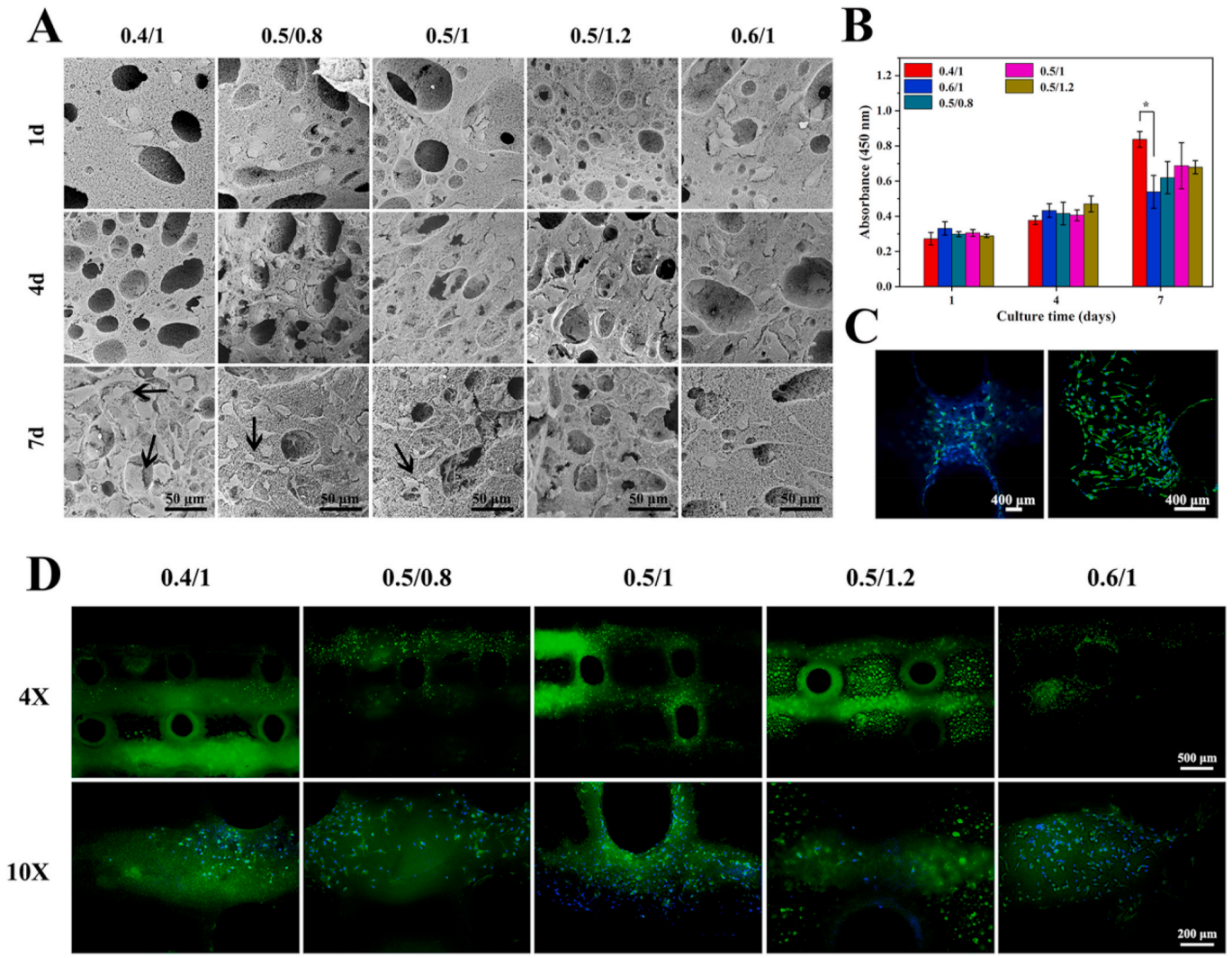

Fig. 4. *In vitro* cell biocompatibility evaluation. (A) SEM images of HUVECs cultured on different scaffolds for 1, 4 and 7 days. (B) HUVECs proliferation on different scaffolds after cultured for 1, 4 and 7 days. (C) Representative confocal images of HUVECs cultured on scaffolds, cytoskeleton stained with Alexa Fluor™ 488 Phalloidin (green) and nuclei stained with DAPI (blue) (Video 2). (D) Fluorescence staining images of HUVECs on the longitudinal section of different scaffolds after 7 days' culture. *P < 0.05.

group showed a better ability to induce HUVECs migration, which may be due to the shorter interval between pores and better connectivity. Therefore, the contact area between the hydrogel and the growth fluid was larger, and the growth factor release rate was relatively faster. In summary, the released VEGF from VEGF-loaded IPMs scaffolds can significantly induce HUVECs migration when the loaded VEGF concentration reaching to 500 ng/mL.

Next, *in vitro* scratch healing experiment was performed to evaluate the induction function on endothelial cell migration. As shown in Fig. 6B. The blank control group and the VEGF-free group showed a small amount of cell migration, while the experimental group with a high concentration of VEGF observed obvious cell migration (Fig. 6B(f, g)). However, in comparison with the 0.5/1 scaffold loading with 500 ng/mL VEGF, it was found that the 0.5/0.8 scaffold loading with 500 ng/mL VEGF showed a better scratch healing effect. The results showed that the released VEGF from VEGF-loaded IPMs scaffolds can stimulate endothelial cell migration in a concentration-dependent manner, and the 0.5/0.8 scaffold loading with 500 ng/mL VEGF exhibited better stimulation effect on endothelial cell migration.

In vivo CAM model is an ideal model for studying angiogenesis of scaffolds, as the CAM membrane has a certain degree of wettability allowing growth factors to be released from hydrogels. The ratio of vascular areas was measured through Image-Pro Plus software after 48 h of incubation, as shown in Fig. 6C. The blood vessels in the VEGF-free group showed normal tree root-like growth, while the blood vessels in the groups with VEGF showed a dense capillary network. Moreover, scaffolds with a concentration of 1000 ng/mL VEGF showed a denser capillary network than scaffolds with a concentration of 500 ng/mL VEGF. By comparing the two groups with high-concentration of VEGF, the 0.5/0.8 group had a better ability to promote vascularization. According to the ratio of the vascular area (Fig. 6C(g)), the 0.5/0.8 group showed a significant increase as compared with the 0.5/1 group in the angiogenesis area at the same concentration ($P < 0.05$). Overall, these results indicated that the VEGF-loaded IPMs scaffolds could promote vascular growth, especially for the 0.5/0.8 group.

3.3. Differentiation ability of VEGF@IPMs scaffold in vitro

To examine the effects of VEGF@IPMs scaffolds on osteogenic differentiation of rBMSCs, quantitative PCR analysis was performed. Fig. 7A–D showed the expression of osteogenic genes including RUNX2, OCN, OPN, and Col I after rBMSCs were cultured with IPMs scaffolds for 7 and 14 days, respectively. After 7 days of induction, the mRNA expression level of these genes in the VEGF@IPMs scaffold group was

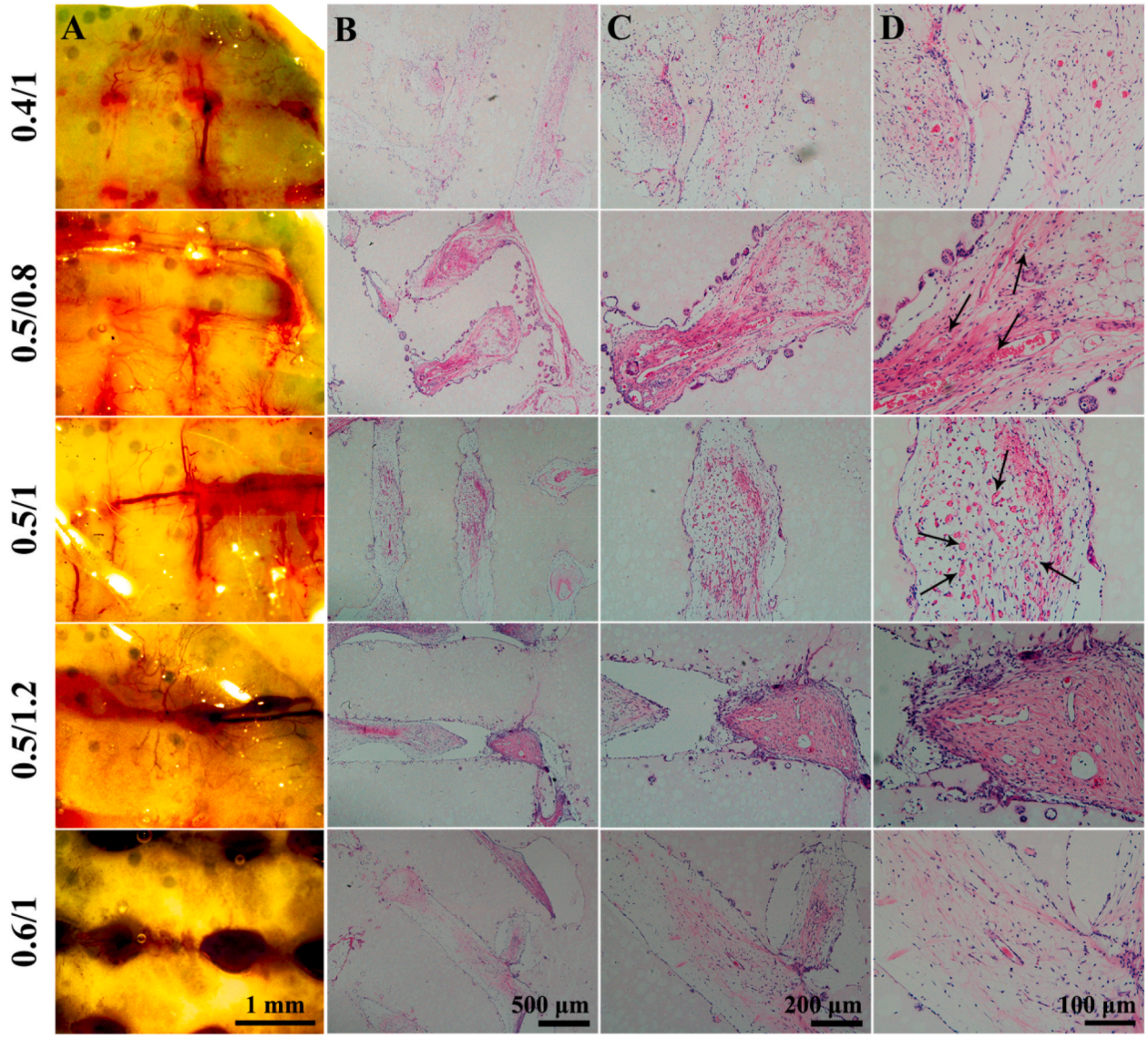

Fig. 5. Evaluation of vascularization after subcutaneous embedding of different scaffolds. (A) Stereo microscope and (B–D) H&E staining of different IPMs scaffolds after subcutaneous implantation in ICR mice for 4 weeks.

significantly increased compared with the control and IPMs scaffold groups ($P < 0.01$). On day 14, we also observed the same result. Compared with the VEGF@0.5/1-IPMs scaffold group, VEGF@0.5/0.8-IPMs scaffold showed higher mRNA expression of these osteogenic markers. Besides, we also detected the angiogenic gene expression after rBMSCs were cultured with IPMs scaffolds for 14 days. It was found that the higher mRNA expression of VEGFR2 and vWF genes was observed in the VEGF-loaded groups, while there was no significant difference between VEGF@0.5/0.8-IPMs scaffold group and VEGF@0.5/1-IPMs scaffold group (Fig. 7F).

3.4. Evaluation of vascularization ability in vivo

The effect of the local growth factor release on the ectopic blood vessel formation was studied by microangiography and μCT imaging after 4 weeks of implantation. The three-dimensional μCT reconstruction images revealed newly formed blood vessels distributed in the implants (Fig. 8A). Compared with other scaffolds, the vascular network within VEGF-containing scaffolds was denser. In the VEGF@0.5/0.8-IPMs scaffold group, the more vascular network was observed, and the blood vessels were extended along the channel within the scaffolds (Video 3). From the quantitative result in Fig. 8B, VEGF@0.5/0.8-IPMs scaffold group had a significantly larger total vessel volume than other groups. The stereomicroscope showed that the vascular supply of the scaffold surface tissue in the VEGF@IPMs scaffold group was more abundant, and the effect was more obvious with the increase of time (Fig. S5). These results were further confirmed by H&E staining (Fig. 8C). After 2 weeks, the IPMs scaffold group showed a minor cell infiltration along the edge of the scaffold, while the VEGF@IPMs scaffold group showed relatively more cell infiltration and more blood vessels. After 4 weeks, the cell infiltration effect in the VEGF@0.5/0.8-IPMs scaffold group was the best, and the enlarged image even showed that the microvessel was invaded in the macropore structure of the PLLA/PCL scaffold.

Supplementary video related to this article can be found at https://doi.org/10.1016/j.bioactmat.2021.02.033

3.5. Evaluation of VEGF@IPMs scaffold bone repair ability in vivo

In situ bone repair was used to further evaluate the effects of VEGF@IPMs scaffold on rat skull repair. The bone formation of each group at 6 and 12 weeks after surgery is shown in Fig. 9A. The μCT reconstruction

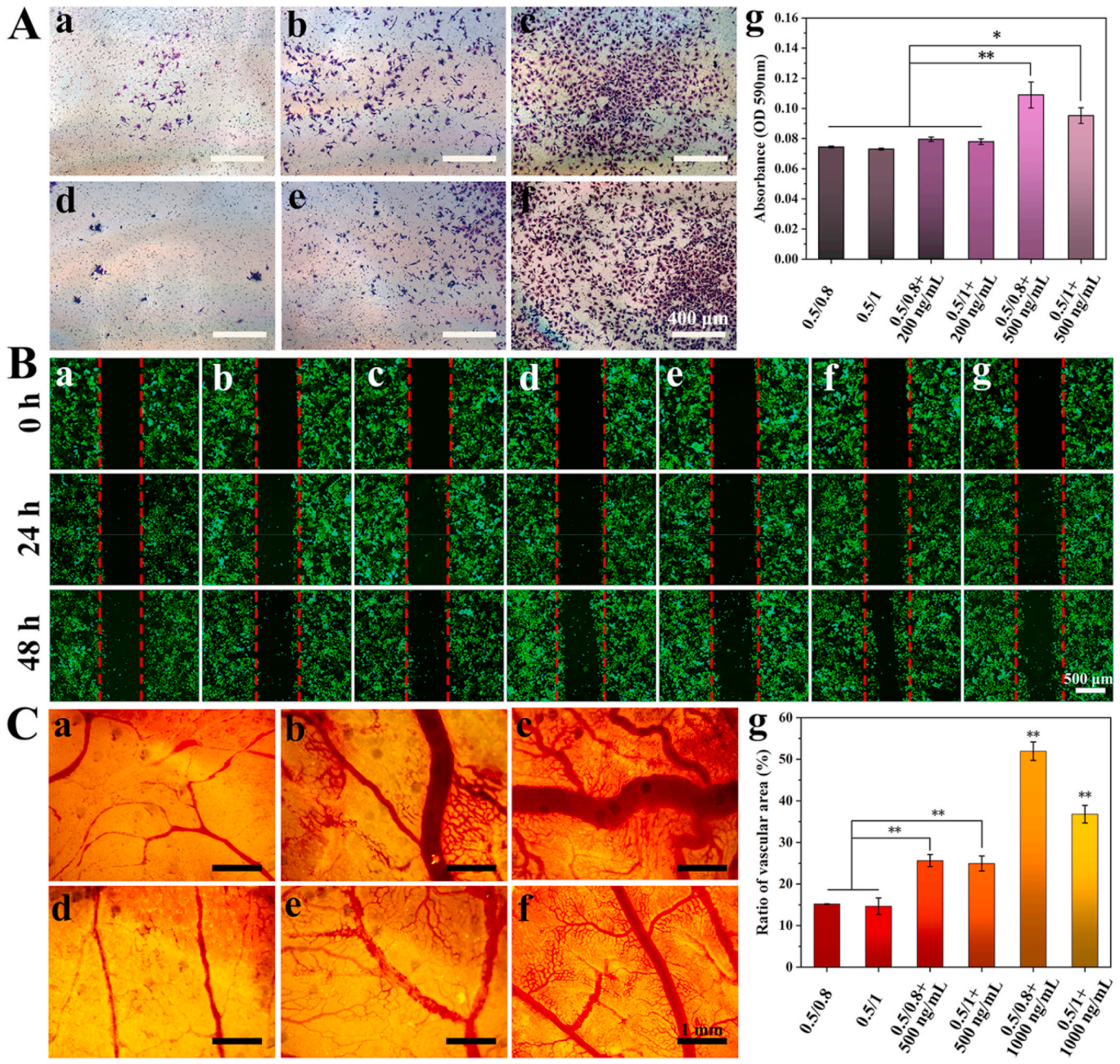

Fig. 6. The migration effects of HUVECs and the pro-angiogenesis effects of different samples in the CAM model. (A) The effects on HUVECs migration in the Transwell assay. (a, b, c) are all 0.5/0.8 hydrogels, the VEGF concentration is 0, 200, and 500 ng/mL, respectively. (d, e, f) are all 0.5/1 hydrogels, the VEGF concentration is 0, 200 and 500 ng/mL. (g) Quantification of the Transwell assay. (B) The effects on HUVECs migration in the scratch wound assay. (a) control, (b, d, f) are all 0.5/0.8 hydrogels, the VEGF concentration is 0, 200 and 500 ng/mL (c, e, g) are all 0.5/1 hydrogels, the VEGF concentration is 0, 200 and 500 ng/mL. (C) Optical images of neo-blood vessel formation after 48 h of treatment with different samples in the CAM model. (a, b, c) are all 0.5/0.8 hydrogels, the VEGF concentration is 0, 500 and 1000 ng/mL (d, e, f) are all 0.5/1 hydrogels, the VEGF concentration is 0, 500 and 1000 ng/mL. (g) The percentage of vascular area. *$P < 0.05$, **$P < 0.01$.

images clearly showed that there was almost no new bone formation in the control group at 6 weeks, while there was an obvious new bone formation in the IPMs and VEGF@IPMs scaffold groups. After 12 weeks, the bone mass of each group increased significantly. The BV/TV in the VEGF@IPMs scaffold group was significantly larger than that in the IPMs scaffold group at 6 weeks ($P < 0.01$), and further increased at 12 weeks (Fig. 9B). Most likely, VEGF enhanced bone formation indirectly by increasing the supportive vascular network and vascular permeability [41,42]. VEGF may play an important role in multiple stages in the process of bone defect repair, and the increase in local blood flow improves the accessibility of cell implantation sites [43]. For example, VEGF promotes the recruitment of macrophages and angiogenesis in the inflammatory phase, and intramembranous osteogenesis also requires the participation of VEGF to promote bone regeneration [44]. Interestingly, at 12 weeks, the bone volume of the VEGF@0.5/0.8-IPMs scaffold group was significantly higher than that of the VEGF@0.5/1-IPMs scaffold group ($P < 0.05$), which may be related to the important role of angiogenesis in bone repair.

Subsequently, H&E staining and Masson's trichrome staining were used to observe the new bone formation after implantation of scaffolds in the bone defect sites. As shown in Fig. 9C, only a small amount of new bone was formed in the control group. In contrast, a large amount of new

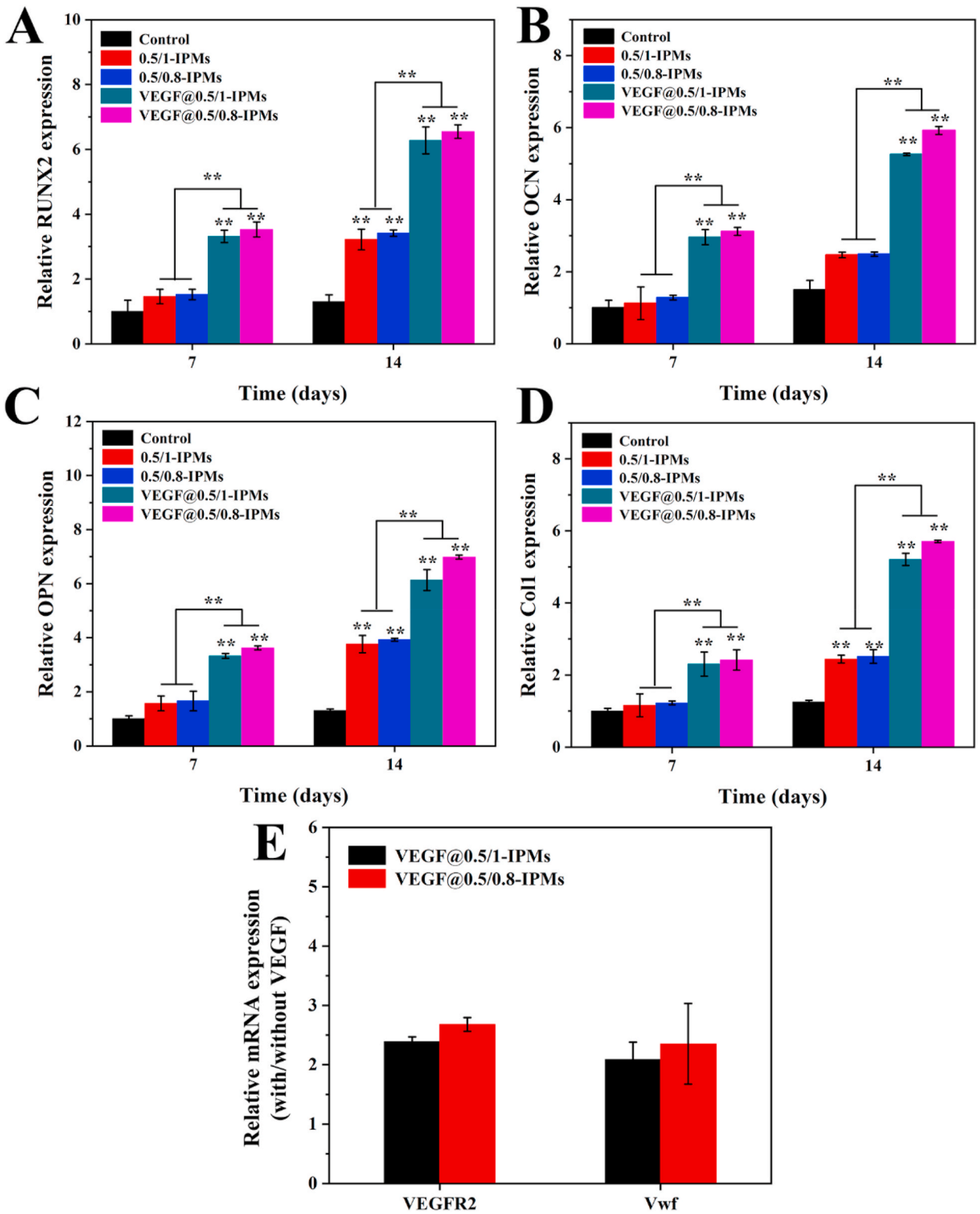

Fig. 7. Quantitative analysis for rBMSCs cultured on IPMs scaffolds for 7 and 14 days. The expression of osteogenic-associated genes including (A) RUNX2, (B) OCN, (C) OPN and (D) Col I in different scaffold groups. (E) The expression of angiogenesis-related genes including VEGFR2 and Vwf in different scaffold groups loading with VEGF. Significant difference compared to the control group, **P < 0.01.

bone formation around the bone defect was observed in the IPMs scaffold group and VEGF@IPMs scaffold group, and the latter was more obvious than the former. Scaffolds with smaller diameters possess more channels in the same mold, which could provide more cell attachment sites due to larger surface area [45]. The porous scaffold recruits osteoprogenitor cells from the adjacent periosteum [46]. When implanted in the defect, the scaffold stimulates and guides these cells to infiltrate the interior of the porous scaffolds [5]. Therefore, the VEGF@0.5/0.8-IPMs scaffold group with more space for cell/tissue ingrowth was in favor of bone tissue formation.

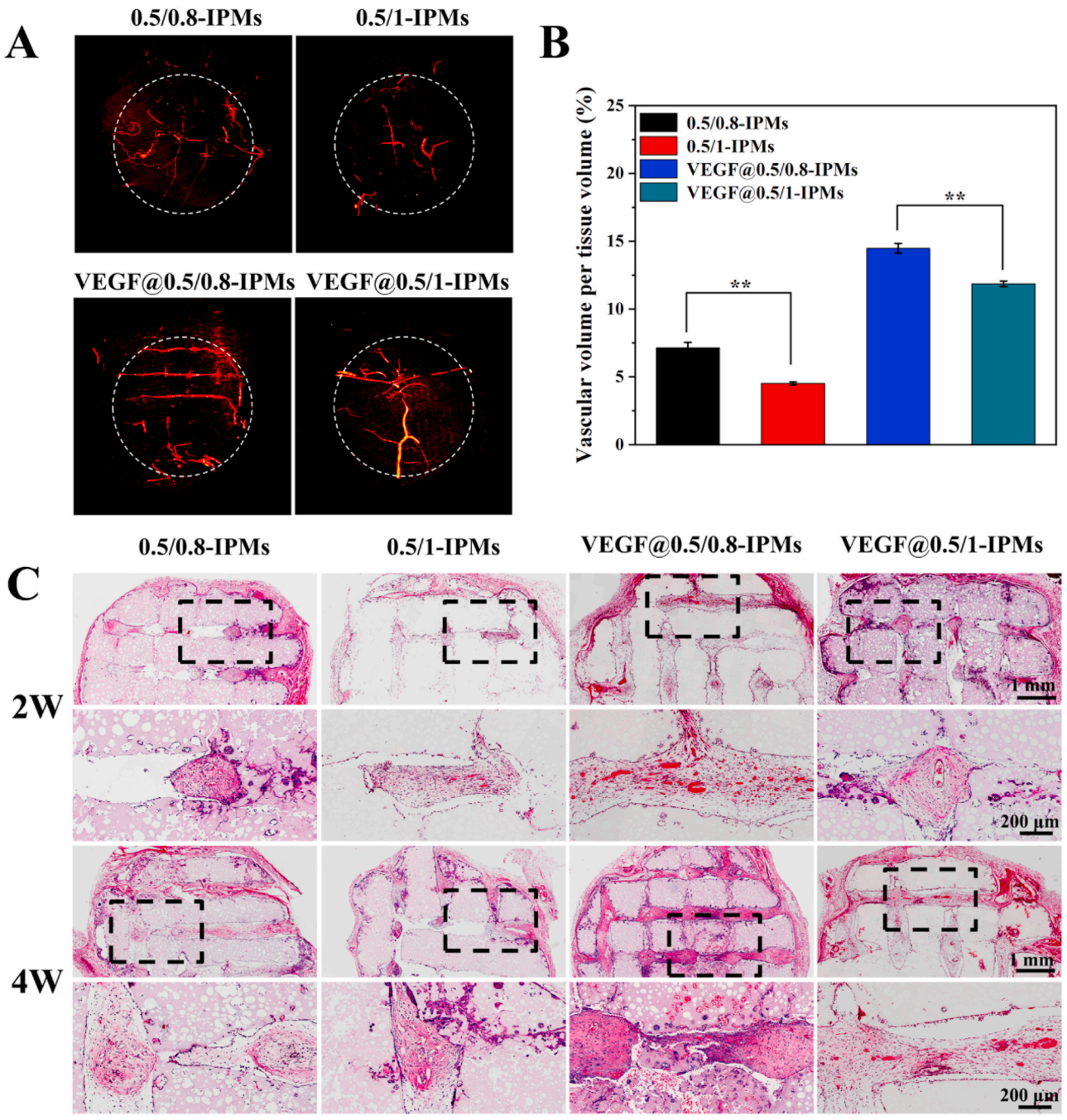

Fig. 8. Analysis of the vascular network formation after implantation for 2 and 4 weeks in ICR mice. (A) 3D-reconstructed μCT images of blood vessels after 4 weeks. (B) Summarized data showing the difference of new vascular volume normalized tissue volume in different groups. (C) Histological observation by H&E staining, the bottom images were the magnified fields. **P < 0.01.

Masson's trichrome staining was used to further assess the newly formed bone, as shown in Fig. 9D. Consistent with the results of H&E staining, in Masson's trichrome staining image, it was observed that the IPMs scaffold group and VEGF@IPMs scaffold group possessed more new bone formation than the control group. Furthermore, the VEGF@0.5/0.8-IPMs scaffold group showed better performance on the bone regeneration compared with the VEGF@0.5/1-IPMs scaffold group.

To investigate the angiogenesis in the process of bone repair, we performed immunofluorescence staining on the endothelial marker CD31 and the vascular smooth muscle marker α-SMA during the formation of new blood vessels, as shown in Fig. 10. The red fluorescence represents CD31, and the green fluorescence represents α-SMA, both of which have a typical circular or elliptical structure. The results showed that almost no new blood vessels were formed in the control group, while a few blood vessels were formed in the IPMs scaffold group. However, compared with other groups, more new blood vessels were formed in the VEGF@IPMs scaffold group. The quantitative results of vessel occupied area indicated that the expression of CD31 and α-SMA in VEGF@0.5/0.8-IPMs scaffold was significantly higher (**P < 0.01) than that of other groups (Fig. 10B and C). Besides, the expression levels of osteoblast markers (OCN and OPN) in VEGF@IPMs scaffold groups were also increased accordingly. Notably, the expression level of OPN and OCN in VEGF@0.5/0.8-IPMs scaffold group was significantly higher than that in VEGF@0.5/1-IPMs scaffold group (Fig. 10D and E). The above results showed that VEGF@0.5/0.8-IPMs scaffold could

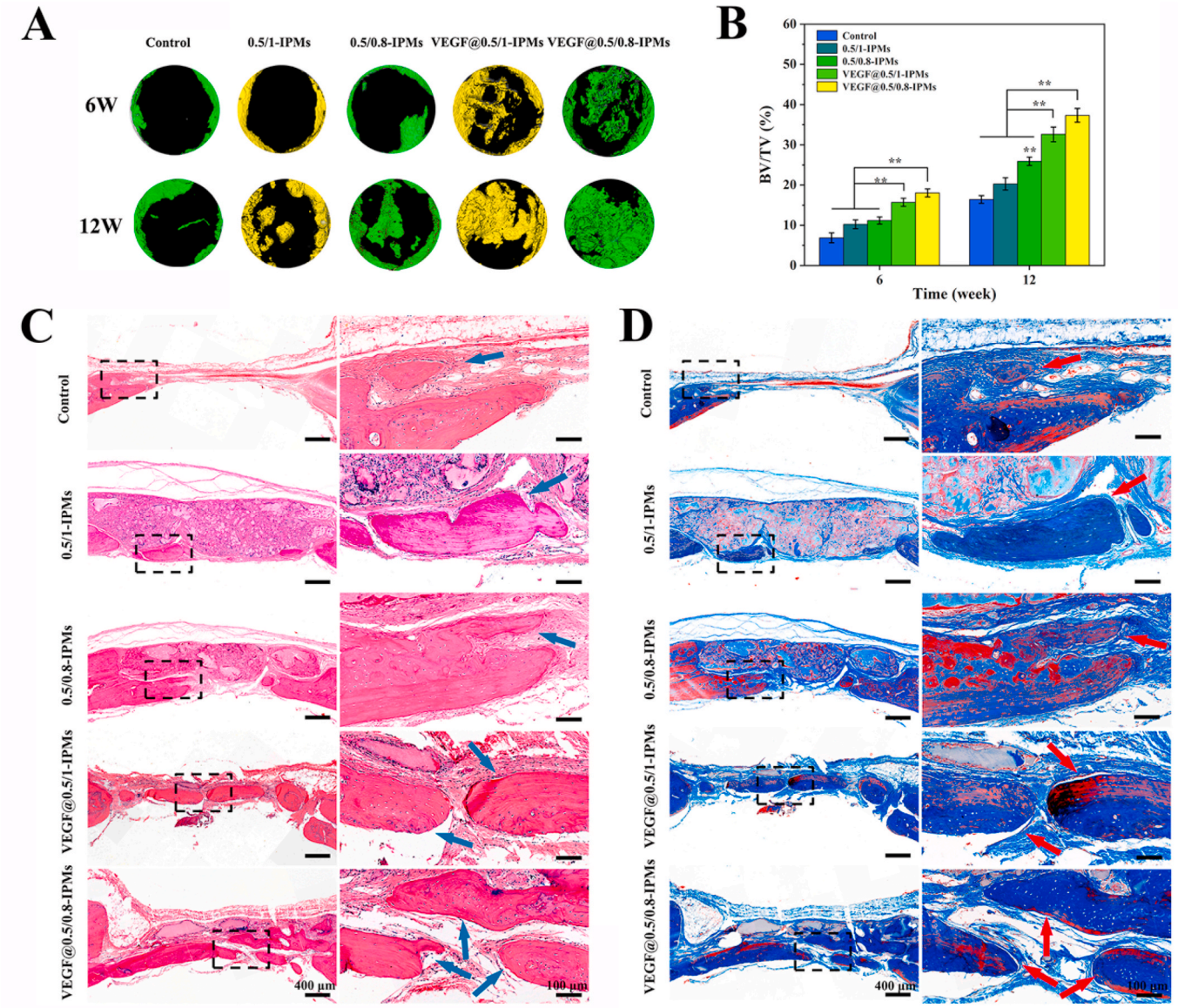

Fig. 9. Micro-CT analysis of the effect of the scaffolds on bone defect regeneration *in vivo*. The identified scaffolds (0.5/1-IPMs, 0.5/0.8-IPMs, VEGF@0.5/1-IPMs and VEGF@0.5/0.8-IPMs) were implanted into the cranial defect of rats. The control group refers to the rat bone defect without treatment. (A) Micro-CT images of rat cranial bone repair after 6 and 12 weeks. (B) The BV/TV of the regenerated tissue was calculated by the CT-Analyzer software after 6 and 12 weeks. (C) H&E staining and Masson's trichrome staining images of new bone formation in the rat cranial bone defects at 12 weeks. The blue and red arrows indicate the new bone. *P < 0.05, **P < 0.01.

significantly enhance the new bone formation by promoting angiogenesis during the process of bone repair [47].

Previous studies have demonstrated that incorporation of microchannels within scaffolds had great contribution on the extent of tissue and vascular ingrowth [7]. For example, Rnjak-Kovacina et al. fabricated the silk-based scaffolds with arrayed hollow channels (254 μm- and 508 μm-diameter). The results of subcutaneous implantation assay indicated that the scaffold with hollow channels showed better cell infiltration compared with the unchanneled scaffold. This was particularly obvious in the scaffold with 508 μm diameter channels [14]. In this work, different microchannel patterns within the scaffolds were made based on 3D printing technology. It is unlikely that a single microchannel design can bring outstanding vascularization. Here, the microchannel within the scaffold can facilitate the transportation of solutes and thereby promoting the tissue ingrowth and vascularization, as well as can provide the space for VEGF loading to further enhance the vascularization. Benefited from the synergistic effect of microchannel networks and VEGF release, more vascular formation was observed in the VEGF@IPMs-0.5/0.8 scaffold. As a result, the bone defect area showed more newly formed bone tissue after the VEGF@0.5/0.8-IPMs scaffold implantation. Therefore, we have proposed an effective strategy on the construction of nanofibrous scaffolds with interconnected perfusable microchannel networks for engineering of vascularized bone tissue.

4. Conclusion

In this study, we successfully prepared a nanofibrous PLLA/PCL scaffold with interconnected perfusion microchannel networks (IPMs) based on 3D printing technology. Furthermore, different diameters and spacings were made to reveal the effect of microchannel structure on angiogenesis and osteogenesis of bone tissue. 0.5/0.8-IPMs (spacing/diameter = 0.5/0.8) and 0.5/1-IPMs (spacing/diameter = 0.5/1) scaffolds were selected for subsequent loading of rhVEGF165, which showed

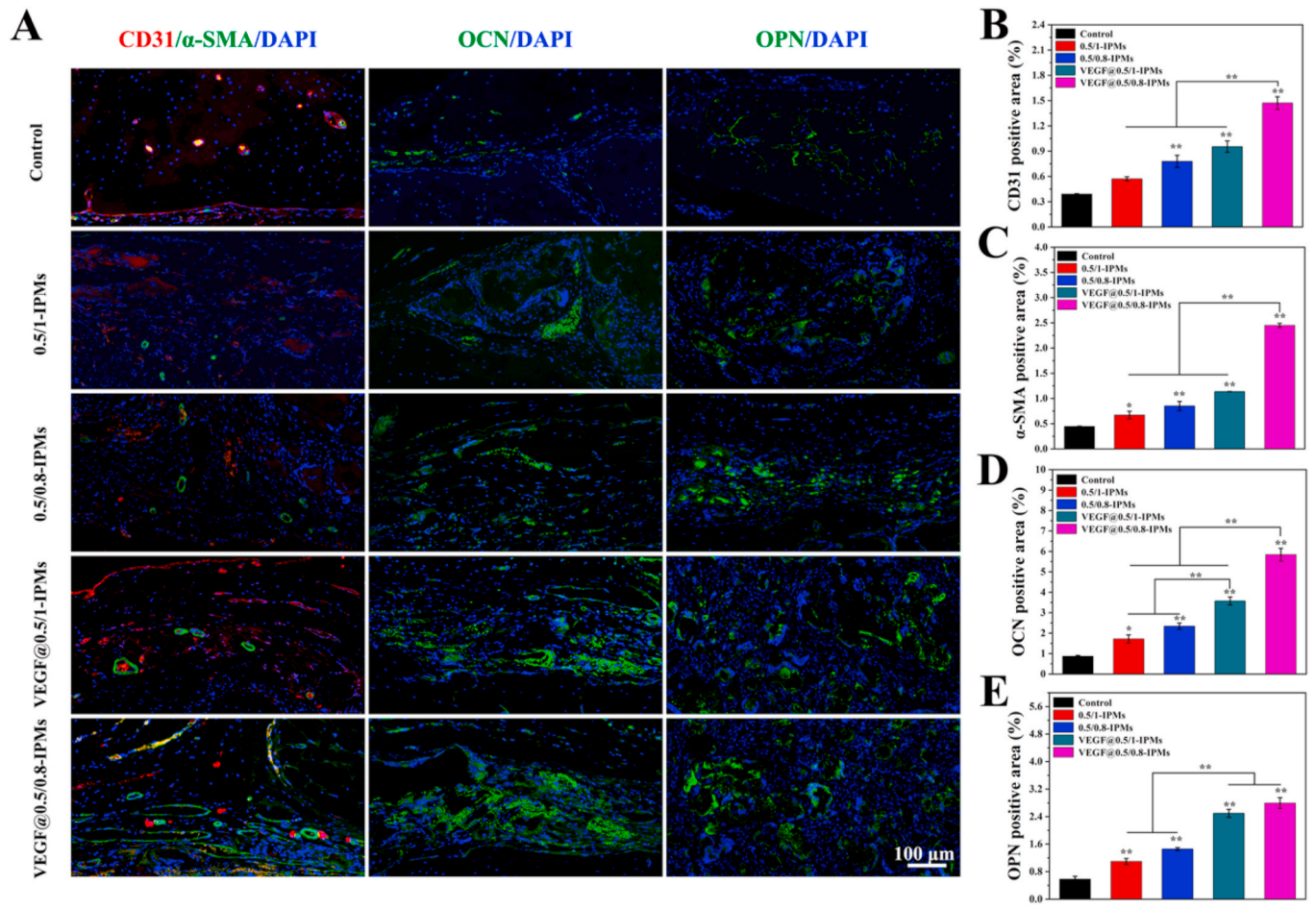

Fig. 10. Representative immunofluorescence staining at 12 weeks. (A) Fluorescence images of CD31 (red), α-SMA (green), OCN (green), OPN (green), and cell nucleus (blue) staining. (B–E) Quantitative analysis of positively stained areas using Image-Pro Plus software. *P < 0.05, **P < 0.01 versus control group.

the deeper cell distribution and richer blood vessel distribution than other groups. The growth factor rhVEGF-165 was loaded in the CMCS/A-HA hydrogel. After 4 weeks of implantation, microangiography was used to analyze angiogenesis, the total vascular volume of VEGF@IPMs-0.5/0.8 scaffold was significantly higher than that of VEGF@IPMs-0.5/1 scaffold. In the rat cranial bone defects experiments, the result indicated that VEGF@IPMs-0.5/0.8 scaffold significantly enhanced new bone formation in the bone defect area. In summary, the strategy is highly versatile to construct microchannel structures within the scaffolds by adjustable caramel-based templates, and the combination of interconnected perfusion microchannel networks and angiogenic factor significantly promote the effects of angiogenesis and bone repair.

CRediT authorship contribution statement

Jiani Gu: Conceptualization, Methodology, Data curation, Formal analysis, Writing – original draft. **Qianqian Zhang:** Investigation, Data curation. **Mengru Geng:** Methodology, Validation. **Weizhong Wang:** Methodology, Investigation. **Jin Yang:** Methodology, Investigation. **Atta ur Rehman Khan:** Writing – review & editing, Formal analysis. **Haibo Du:** Methodology, Formal analysis. **Zhou Sha:** Methodology, Data curation. **Xiaojun Zhou:** Funding acquisition, Conceptualization, Validation, Supervision. **Chuanglong He:** Funding acquisition, Conceptualization, Writing – review & editing, Project administration.

Declaration of competing interest

The authors declare no conflict of interest.

Acknowledgements

This work was financially supported by the National Key Research and Development Program of China (2018YFB1105602), National Natural Science Foundation of China (32071350, 31771048, 81702124), Fundamental Research Funds for the Central Universities (2232018A3-07, 2232019A3-06), International Cooperation Fund of the Science and Technology Commission of Shanghai Municipality (19440741600).

Appendix A. Supplementary data

Supplementary data to this article can be found online at https://doi.org/10.1016/j.bioactmat.2021.02.033.

References

[1] D. Steiner, F. Lampert, G.B. Stark, G. Finkenzeller, Effects of endothelial cells on proliferation and survival of human mesenchymal stem cells and primary osteoblasts, J. Orthop. Res. 30 (10) (2012) 1682–1689.
[2] X.F. Ye, L. Lu, M.E. Kolewe, K. Hearon, K.M. Fischer, J. Coppeta, L.E. Freed, Scalable units for building cardiac tissue, Adv. Mater. 26 (42) (2014) 7202–7208.
[3] P. Blinder, P.S. Tsai, J.P. Kaufhold, P.M. Knutsen, H. Suhl, D. Kleinfeld, The cortical angiome: an interconnected vascular network with noncolumnar patterns of blood flow, Nat. Neurosci. 16 (7) (2013), 889-U150.
[4] W. Jia, P.S. Gungor-Ozkerim, Y.S. Zhang, K. Yue, K. Zhu, W. Liu, Q. Pi, B. Byambaa, M.R. Dokmeci, S.R. Shin, A. Khademhosseini, Direct 3D bioprinting of perfusable vascular constructs using a blend bioink, Biomaterials 106 (2016) 58–68.
[5] J. Diao, J. OuYang, T. Deng, X. Liu, Y. Feng, N. Zhao, C. Mao, Y. Wang, 3D-Plotted beta-tricalcium phosphate scaffolds with smaller pore sizes improve in vivo bone regeneration and biomechanical properties in a critical-sized calvarial defect rat model, Adv. Healthc. Mater. 7 (17) (2018), e1800441.

[6] N.A. Sears, D.R. Seshadri, P.S. Dhavalikar, E. Cosgriff-Hernandez, A review of three-dimensional printing in tissue engineering, Tissue Eng. B Rev. 22 (4) (2016) 298–310.
[7] K.S. Lim, M. Baptista, S. Moon, T.B.F. Woodfield, J. Rnjak-Kovacina, Microchannels in development, survival, and vascularisation of tissue analogues for regenerative medicine, Trends Biotechnol. 37 (11) (2019) 1189–1201.
[8] E.S. Place, N.D. Evans, M.M. Stevens, Complexity in biomaterials for tissue engineering, Nat. Mater. 8 (6) (2009) 457–470.
[9] A. Lisovsky, M.D. Chamberlain, L.A. Wells, M.V. Sefton, Cell interactions with vascular regenerative MAA-based materials in the context of wound healing, Adv. Healthc. Mater. 4 (16) (2015) 2375–2387.
[10] L.R. Madden, D.J. Mortisen, E.M. Sussman, S.K. Dupras, J.A. Fugate, J.L. Cuy, K. D. Hauch, M.A. Laflamme, C.E. Murry, B.D. Ratner, Proangiogenic scaffolds as functional templates for cardiac tissue engineering, Proc. Natl. Acad. Sci. U. S. A. 107 (34) (2010) 15211–15216.
[11] S.A. Biela, Y. Su, J.P. Spatz, R. Kemkemer, Different sensitivity of human endothelial cells, smooth muscle cells and fibroblasts to topography in the nano-micro range, Acta Biomater. 5 (7) (2009) 2460–2466.
[12] M.F.A. Cutiongco, S.H. Goh, R. Aid-Launais, C. Le Visage, H.Y. Low, E.K.F. Yim, Planar and tubular patterning of micro and nano-topographies on poly(vinyl alcohol) hydrogel for improved endothelial cell responses, Biomaterials 84 (2016) 184–195.
[13] V. Karageorgiou, D. Kaplan, Porosity of 3D biomaterial scaffolds and osteogenesis, Biomaterials 26 (27) (2005) 5474–5491.
[14] J. Rnjak-Kovacina, L.S. Wray, J.M. Golinski, D.L. Kaplan, Arrayed hollow channels in silk-based scaffolds provide functional outcomes for engineering critically-sized tissue constructs, Adv. Funct. Mater. 24 (15) (2014) 2188–2196.
[15] W. Zhang, L.S. Wray, J. Rnjak-Kovacina, L. Xu, D. Zou, S. Wang, M. Zhang, J. Dong, G. Li, D.L. Kaplan, X. Jiang, Vascularization of hollow channel-modified porous silk scaffolds with endothelial cells for tissue regeneration, Biomaterials 56 (2015) 68–77.
[16] H.W. Kang, S.J. Lee, I.K. Ko, C. Kengla, J.J. Yoo, A. Atala, A 3D bioprinting system to produce human-scale tissue constructs with structural integrity, Nat. Biotechnol. 34 (3) (2016) 312–319.
[17] D.B. Kolesky, R.L. Truby, A.S. Gladman, T.A. Busbee, K.A. Homan, J.A. Lewis, 3D bioprinting of vascularized, heterogeneous cell-laden tissue constructs, Adv. Mater. 26 (19) (2014) 3124–3130.
[18] R. Xie, W. Zheng, L. Guan, Y. Ai, Q. Liang, Engineering of hydrogel materials with perfusable microchannels for building vascularized tissues, Small 16 (15) (2020), e1902838.
[19] L.L. Ouyang, J.P.K. Armstrong, Q. Chen, Y.Y. Lin, M.M. Stevens, Void-free 3D bioprinting for in situ endothelialization and microfluidic perfusion, Adv. Funct. Mater. 30 (1) (2020).
[20] L. Shao, Q. Gao, C. Xie, J. Fu, M. Xiang, Y. He, Directly coaxial 3D bioprinting of large-scale vascularized tissue constructs, Biofabrication 12 (3) (2020), 035014.
[21] D. Lei, Y. Yang, Z.H. Liu, B.Q. Yang, W.H. Gong, S. Chen, S.F. Wang, L.J. Sun, B. Y. Song, H.X. Xuan, X.M. Mo, B.B. Sun, S. Li, Q. Yang, S.X. Huang, S.Y. Chen, Y. D. Ma, W.G. Liu, C.L. He, B. Zhu, E.M. Jeffries, F.L. Qing, X.F. Ye, Q. Zhao, Z. W. You, 3D printing of biomimetic vasculature for tissue regeneration, Mater. Horiz. 6 (6) (2019) 1197–1206.
[22] Y. Liu, S. Yang, L. Cao, X. Zhang, J. Wang, C. Liu, Facilitated vascularization and enhanced bone regeneration by manipulation hierarchical pore structure of scaffolds, Mater. Sci. Eng. C Mater. Biol. Appl. 110 (2020) 110622.
[23] W. Wang, W. Nie, X. Zhou, W. Feng, L. Chen, Q. Zhang, Z. You, Q. Shi, C. Peng, C. He, Fabrication of heterogeneous porous bilayered nanofibrous vascular grafts by two-step phase separation technique, Acta Biomater. 79 (2018) 168–181.
[24] M.T. Poldervaart, H. Gremmels, K. van Deventer, J.O. Fledderus, F.C. Oner, M. C. Verhaar, W.J. Dhert, J. Alblas, Prolonged presence of VEGF promotes vascularization in 3D bioprinted scaffolds with defined architecture, J. Contr. Release 184 (2014) 58–66.
[25] H. Tan, C.R. Chu, K.A. Payne, K.G. Marra, Injectable in situ forming biodegradable chitosan-hyaluronic acid based hydrogels for cartilage tissue engineering, Biomaterials 30 (13) (2009) 2499–2506.
[26] S.D. Nath, C. Abueva, B. Kim, B.T. Lee, Chitosan-hyaluronic acid polyelectrolyte complex scaffold crosslinked with genipin for immobilization and controlled release of BMP-2, Carbohydr. Polym. 115 (2015) 160–169.
[27] D.B. Pike, S. Cai, K.R. Pomraning, M.A. Firpo, R.J. Fisher, X.Z. Shu, G.D. Prestwich, R.A. Peattie, Heparin-regulated release of growth factors in vitro and angiogenic response in vivo to implanted hyaluronan hydrogels containing VEGF and bFGF, Biomaterials 27 (30) (2006) 5242–5251.
[28] I.R. Serra, R. Fradique, M.C. Vallejo, T.R. Correia, S.P. Miguel, I.J. Correia, Production and characterization of chitosan/gelatin/beta-TCP scaffolds for improved bone tissue regeneration, Mater. Sci. Eng. C Mater. Biol. Appl. 55 (2015) 592–604.
[29] R. Zhang, P.X. Ma, Poly(alpha-hydroxyl acids)/hydroxyapatite porous composites for bone-tissue engineering. I. Preparation and morphology, J. Biomed. Mater. Res. 44 (4) (1999) 446–455.
[30] M.H. Pourgholami, L.M. Khachigian, R.G. Fahmy, S. Badar, L. Wang, S.W. Chu, D. L. Morris, Albendazole inhibits endothelial cell migration, tube formation, vasopermeability, VEGF receptor-2 expression and suppresses retinal neovascularization in ROP model of angiogenesis, Biochem. Biophys. Res. Commun. 397 (4) (2010) 729–734.
[31] Y. Pan, Q. Wu, L. Qin, J. Cai, B. Du, Gold nanoparticles inhibit VEGF165-induced migration and tube formation of endothelial cells via the Akt pathway, BioMed Res. Int. 2014 (2014) 418624.
[32] H. Izuta, Y. Chikaraishi, M. Shimazawa, S. Mishima, H. Hara, 10-Hydroxy-2-decenoic acid, a major fatty acid from royal jelly, inhibits VEGF-induced angiogenesis in human umbilical vein endothelial cells, Evid. Based Complement. Alternat. Med. 6 (4) (2009) 489–494.
[33] A. Taktak-BenAmar, M. Morjen, H. Ben Mabrouk, R. Abdelmaksoud-Dammak, M. Guerfali, N. Fourati-Masmoudi, N. Marrakchi, A. Gargouri, Expression, purification and functionality of bioactive recombinant human vascular endothelial growth factor VEGF165 in E. coli, Amb. Express 7 (1) (2017) 33.
[34] S. Singh, B.M. Wu, J.C. Dunn, Delivery of VEGF using collagen-coated polycaprolactone scaffolds stimulates angiogenesis, J. Biomed. Mater. Res. 100 (3) (2012) 720–727.
[35] W. Yu, T.W. Sun, Z. Ding, C. Qi, H. Zhao, F. Chen, Z. Shi, Y.J. Zhu, D. Chen, Y. He, Copper-doped mesoporous hydroxyapatite microspheres synthesized by a microwave-hydrothermal method using creatine phosphate as an organic phosphorus source: application in drug delivery and enhanced bone regeneration, J. Mater. Chem. B 5 (5) (2017) 1039–1052.
[36] D.D. Kitts, C.H. Wu, A. Kopec, T. Nagasawa, Chemistry and genotoxicity of caramelized sucrose, Mol. Nutr. Food Res. 50 (12) (2006) 1180–1190.
[37] Z.P. Zhang, J. Hu, P.X. Ma, Nanofiber-based delivery of bioactive agents and stem cells to bone sites, Adv. Drug Deliv. Rev. 64 (12) (2012) 1129–1141.
[38] T. Elsdale, J. Bard, Collagen substrata for studies on cell behavior, J. Cell Biol. 54 (3) (1972) 626–637.
[39] J.H. Jeong, V. Chan, C. Cha, P. Zorlutuna, C. Dyck, K.J. Hsia, R. Bashir, H. Kong, Living" microvascular stamp for patterning of functional neovessels; orchestrated control of matrix property and geometry, Adv. Mater. 24 (1) (2012) 58–63, 51.
[40] J. Lienau, K. Schmidt-Bleek, A. Peters, F. Haschke, G.N. Duda, C. Perka, H.J. Bail, N. Schutze, F. Jakob, H. Schell, Differential regulation of blood vessel formation between standard and delayed bone healing, J. Orthop. Res. 27 (9) (2009) 1133–1140.
[41] N. Hansen-Algenstaedt, C. Joscheck, L. Wolfram, C. Schaefer, I. Muller, A. Bottcher, G. Deuretzbacher, L. Wiesner, M. Leunig, P. Algenstaedt, W. Ruther, Sequential changes in vessel formation and micro-vascular function during bone repair, Acta Orthop. 77 (3) (2006) 429–439.
[42] G. Neufeld, T. Cohen, S. Gengrinovitch, Z. Poltorak, Vascular endothelial growth factor (VEGF) and its receptors, Faseb. J. 13 (1) (1999) 9–22.
[43] S. Otsuru, K. Tamai, T. Yamazaki, H. Yoshikawa, Y. Kaneda, Bone marrow-derived osteoblast progenitor cells in circulating blood contribute to ectopic bone formation in mice, Biochem. Biophys. Res. Commun. 354 (2) (2007) 453–458.
[44] K. Hu, B.R. Olsen, Osteoblast-derived VEGF regulates osteoblast differentiation and bone formation during bone repair, J. Clin. Invest. 126 (2) (2016) 509–526.
[45] F.S.L. Bobbert, A.A. Zadpoor, Effects of bone substitute architecture and surface properties on cell response, angiogenesis, and structure of new bone, J. Mater. Chem. B 5 (31) (2017) 6175–6192.
[46] R. Cancedda, P. Giannoni, M. Mastrogiacomo, A tissue engineering approach to bone repair in large animal models and in clinical practice, Biomaterials 28 (29) (2007) 4240–4250.
[47] F. Zhao, B. Lei, X. Li, Y. Mo, R. Wang, D. Chen, X. Chen, Promoting in vivo early angiogenesis with sub-micrometer strontium-contained bioactive microspheres through modulating macrophage phenotypes, Biomaterials 178 (2018) 36–47.